The Astrophysical Journal, 809:58 (13pp), 2015 August 10 doi:10.1088/0004-637X/809/1/58

PLASMA PHYSICAL PARAMETERS ALONG CME-DRIVEN SHOCKS. II. OBSERVATION–SIMULATION COMPARISON

F. Bacchini[1], R. Susino[2], A. Bemporad[2], and G. Lapenta[1]
[1] Center for mathematical Plasma Astrophysics (CmPA), KU Leuven, Celestijnenlaan 200B, 3001 Leuven, Belgium; fabio.bacchini@wis.kuleuven.be
[2] Istituto Nazionale di Astrofisica (INAF), Osservatorio Astronomico di Torino, Strada Osservatorio 20, I-10025 Pino Torinese, Torino, Italy; bemporad@oato.inaf.it
Received 2015 May 14; accepted 2015 June 24; published 2015 August 10

ABSTRACT

In this work, we compare the spatial distribution of the plasma parameters along the 1999 June 11 coronal mass ejection (CME)-driven shock front with the results obtained from a CME-like event simulated with the FLIPMHD3D code, based on the FLIP-MHD particle-in-cell method. The observational data are retrieved from the combination of white-light coronagraphic data (for the upstream values) and the application of the Rankine–Hugoniot equations (for the downstream values). The comparison shows a higher compression ratio X and Alfvénic Mach number M_A at the shock nose, and a stronger magnetic field deflection d toward the flanks, in agreement with observations. Then, we compare the spatial distribution of M_A with the profiles obtained from the solutions of the shock adiabatic equation relating M_A, X, and θ_{Bn} (the angle between the upstream magnetic field and the shock front normal) for the special cases of parallel and perpendicular shock, and with a semi-empirical expression for a generically oblique shock. The semi-empirical curve approximates the actual values of M_A very well, if the effects of a non-negligible shock thickness δ_{sh} and plasma-to magnetic pressure ratio β_u are taken into account throughout the computation. Moreover, the simulated shock turns out to be supercritical at the nose and sub-critical at the flanks. Finally, we develop a new one-dimensional Lagrangian ideal MHD method based on the GrAALE code, to simulate the ion-electron temperature decoupling due to the shock transit. Two models are used, a simple solar wind model and a variable-γ model. Both produce results in agreement with observations, the second one being capable of introducing the physics responsible for the additional electron heating due to secondary effects (collisions, Alfvén waves, etc.).

Key words: magnetohydrodynamics (MHD) – shock waves – Sun: coronal mass ejections (CMEs)

1. INTRODUCTION

Coronal mass ejections (CMEs) are large-scale releases of solar material that erupt from the Sun (e.g., Gopalswamy 2003; Forbes et al. 2006). Fast CMEs ($v_{CME} > 800$ km s^{-1}) often drive coronal shock waves, when the local plasma density and magnetic field strength met by the CME are such that the wave front speed exceeds the local Alfvén speed (Gopalswamy 2003).

It is now well known that coronal shocks can accelerate electrons (Schwartz et al. 2011), protons (Park et al. 2012), and ions (e.g., Giacalone 2005), giving origin to gradual bursts of extremely energetic particles, referred to as solar energetic particle (SEP) events, which generally have higher fluxes and harder energetic spectra (Cliver et al. 2004) than impulsive SEPs produced in solar flares. Moreover, shocks propagating into the interplanetary space toward the Earth can carry a significant southward component of the magnetic field that can eventually reconnect with the Earth magnetosphere triggering electromagnetic disturbances at the ground (the so-called geomagnetic storms). For these reasons and because of the severe consequences on human technologies and the terrestrial environment, these phenomena can possibly lead to (e.g., Balan et al. 2014), deepening our understanding of the origin, propagation and physical properties of CME-driven shocks is fundamental in the perspective of space weather forecasting applications.

Over the last decade, many works focused on the signatures of CME-driven shocks in white-light (WL) observations, namely from the *Solar and Heliospheric Observatory* (*SOHO*)/LASCO C2 and C3 coronagraphs and the *STEREO*/COR1 and COR2 telescopes (Sheeley et al. 2000; Vourlidas et al. 2003, 2013; Gopalswamy et al. 2009; Ontiveros & Vourlidas 2009; Gopalswamy & Yashiro 2011; Kim et al. 2012; Lee et al. 2014). WL data have proven to contain much more information than previously thought, and were used with various techniques to derive shock speeds, shock compression ratios $X = \rho_d/\rho_u$ (i.e., the ratio between the upstream ρ_u and the downstream ρ_d plasma densities), geometrical properties of the shock fronts, as well as the strength of the coronal magnetic field encountered by the shocks, and also allowed studies on the correlation between the SEP fluxes and associated CME speeds (e.g., Kahler 2001).

Further information on coronal shocks have been obtained by taking advantage of simultaneous multi-wavelength observations, like radio, WL, and ultraviolet (UV). For instance, analyses of the relative position of the shock waves in WL images and the associated radio emission, the so-called type-II radio bursts, which are produced by the accelerated electrons that radiate at the local plasma frequency or its harmonics in the metric and decimetric radio domain and are considered as the manifestations of propagating shock waves, provided spatial information about the actual location of particle acceleration and revealed that the emission in most cases appears far from the shock leading edge, i.e., close to the flanks (Magdalenić et al. 2014), particularly in the enhanced density interaction regions between shocks and streamers (Reiner et al. 2003; Shen et al. 2013). However, whether or not type-II radio bursts originate from the nose of shocks is still a subject of open debate.

Spectroscopic data from *SOHO*/UVCS allowed to supply the kinematical and geometrical information available from WL observations, with the complementary measure of the shock

plasma temperatures, thus providing information on the shock plasma heating (e.g., Mancuso et al. 2002; Mancuso & Avetta 2008). Moreover, these parameters can be reliably used together with the MHD Rankine–Hugoniot (RH) equations (see, e.g., Treumann 2009) for the general case of oblique shocks to determine both the pre- and post-shock magnetic and velocity field vectors, projected on the plane of the sky. This method has been applied by Bemporad & Mancuso (2010, 2011, 2013) in a few specific events leading to the conclusion that plasma compression is higher at the shock nose, where derived post-shock plasma parameters can be very well approximated with those expected from a parallel shock, and where also conditions of super-criticality were most likely achieved, at least in the early phases of evolution (i.e., at low altitudes in the corona). Conversely, quasi-perpendicular and sub-critical conditions turned out to be characteristic of regions located at the shock flanks. It has been demonstrated, on the other hand, that regions where the shock is super-critical (i.e., where the Alfvénic Mach number exceeds a critical value) are very probable locations for SEP acceleration (see, e.g., Treumann 2009).

In our previous paper (Bemporad et al. 2014, hereafter Paper I) we extended these works using the same technique applied to different points located along the same shock front and found the additional result that the transit of the shock induces a significant deflection of the magnetic field near the shock center, and a smaller deflection at the flanks, implying a draping of the field lines around the expanding CME. Moreover, the propagation of the shock across the upstream corona, assumed to be in thermodynamic equilibrium, is found to cause a decoupling between proton and electron temperatures, with $T_p > T_e$ in the post-shock plasma. The downstream plasma temperatures derived with the RH equations are more representative of post-shock proton temperatures, while temperatures obtained by adiabatic compression are more representative of post-shock electron temperatures (see Paper I).

All these results are in nice agreement with those recently obtained with numerical simulations of CME-driven shock waves. Liu et al. (2011) used the Space Weather Modeling Framework (SWMF; Tóth et al. 2005), a 3D magnetohydrodynamic (MHD) simulation code, to simulate the propagation of CMEs and the associated shocks and found that near the Sun the magnetic field lines drape around the flux rope (the CME ejecta) and align themselves with the magnetic field in the flux rope. More recently, Manchester et al. (2012) and Jin et al. (2012, 2013) implemented the two-temperature (2T) model of van der Holst et al. (2010) in the MHD BATS-R-US code (Powell et al. 1999) within the SWMF. They demonstrated that most of the 2T model outputs can fit WL observations of CME-driven shocks by LASCO C2 and STEREO very well. In particular, they showed that 2T plasma protons are heated up to ~90 MK, and 2T shocks have larger Alfvénic Mach numbers (up to a factor of ~1.4) with respect to the simple one-temperature case. This confirms that CME-driven shocks are supersonic only with respect to the protons, and that only protons are expected to be significantly heated by the transit of the shock (Giacalone 2005; Treumann 2009). Hybrid simulations of a super-Alfvénic quasi-parallel shock, which have the advantage of studying the shock propagation on the ion timescale and of being localized in space in comparison with MHD simulations, were performed by Gargaté et al. (2014), who found that electromagnetic Alfvén waves are generated at the shock front by the counter-streaming ions of the solar wind plasma. The simulations show that a significant number of particles reflected at the shock front interact with the previously formed waves and accelerate, gaining energy up to ~200 MeV, consistent with observations.

The encouraging agreement between the observational results reported in Paper I (and references above) and the numerical studies considered so far deserves further investigation. To this end, in this work we present two numerical simulation approaches, a two-dimensional (2D) particle-in-cell (PIC) MHD approach based on the FLIPMHD3D tool and a one-dimensional (1D) two-temperature MHD approach based on the upgraded version of the GrAALE, in an attempt to reproduce the above constraints and to provide important insights into the physics at the base of CME-driven shock formation and propagation.

2. SUMMARY OF PREVIOUS RESULTS

We refer the reader to Paper I for a detailed description of the data analysis and discussion of the results. Here we mention only that WL images from the LASCO C2 coronagraph relevant to the shock wave driven by the 1999 June 11 CME were used to derive all along the shock front identified in the frame at 11.26 UT the plasma compression ratio X, the angle $\theta_{\rm sh}$ between the normal to the shock front and the radial direction, the shock speed $v_{\rm sh}$, as well as the upstream coronal density ρ_u from the last polarized brightness image acquired by LASCO C2 before the CME.

Synoptic observations acquired before the CME by UVCS were also analyzed in order to provide the missing pre-shock plasma temperatures (of both electrons and protons) and outflow velocities, representative of the upstream coronal plasma met by the shock wave. These parameters were derived from the spectral profiles of the H I Lyα and the O VI $\lambda\lambda$ 1031, 1037 Å doublet lines, in three coronal regions located where the shock front crossed the UVCS field of view (see Figure 3 of Paper I). By combining all these information into the MHD RH equations for the general case of oblique shock we were able to estimate the full set of pre- and post-shock plasma parameters, which are summarized in Table 1 (taken from Table 2 of Paper I) for the two points located at the shock flanks (points 1 and 2) and for the shock nose (point 3).

In the table, T is the temperature, n is the particle density, B is the magnetic field strength, u is the plasma speed in the reference frame at rest with the shock, $\theta_{\rm B}$ is the angle between the shock normal and the magnetic field, θ_u is the angle between the shock normal and the plasma velocity, θ_w is the angle between the shock normal and the plasma velocity in the reference frame at rest with the Sun, $v_{\rm A}$ is the Alfvén speed, c_S is the sound speed, and $u_{\rm out}$ is the plasma speed in the reference frame at rest with the Sun.

3. MODELING APPROACH

3.1. FLIPMHD3D: 2D, Lagrangian, PIC MHD

FLIPMHD3D is a computational tool for PIC visco-resistive MHD based on the FLIP-MHD method developed by Brackbill (see Brackbill & Ruppel 1986 and Brackbill 1991). The code is designed to solve the resistive MHD equations (here in

Table 1
Summary of Plasma Physical Parameters for the Three Points Along the Shock Front Selected for the 1D Simulation Comparison

Point	T (MK)	n (cm^{-3})	B (G)	u (kms^{-1})	θ_B (°)	θ_u (°)	θ_w (°)	v_A (kms^{-1})	c_s (kms^{-1})	u_{out} (kms^{-1})
1 (u)	1.68	4.22×10^5	0.241	1328.3	−54.50	−1.46	−54.50	809.3	215.1	41.7
1 (d)	4.45	7.47×10^5	0.416	788.8	−70.33	−19.92	24.30	1049.5	349.7	653.2
2 (u)	1.02	1.05×10^6	0.511	1281.2	32.60	1.61	32.60	1089.6	167.6	66.7
2 (d)	1.68	1.30×10^6	0.627	1078.8	46.66	16.79	−45.70	1199.1	215.0	435.3
3 (u)	1.49	2.95×10^5	0.205	1455.0	5.17	0.25	5.17	824.2	202.6	70.4
3 (d)	18.40	8.05×10^5	0.330	765.8	51.71	45.89	−29.00	800.88	711.6	1134.3

Note. The upstream (u) values are taken from Paper I, while the downstream (d) values are computed from the standard MHD RH relations for oblique shocks (see text).

Table 2
Comparison Between the Temperature Jumps Obtained with the Two Models, for Both Electrons and Protons

Point	Species	Simple Solar Wind Model			Variable γ Model		
		γ	T_d/T_u	$\bar{T}_d/T_u$	γ	T_d/T_u	$\bar{T}_d/T_u$
1	e	5/3	1.47	2.88	1.13	1.55	2.66
	p	5/3	4.33		1.57	3.77	
2	e	5/3	1.16	1.54	1.13	1.17	1.47
	p	5/3	1.91		1.57	1.77	
3	e	5/3	1.95	12.35	1.13	4.28	11.56
	p	5/3	22.82		1.57	18.85	

Note. The average temperature jump $\bar{T}_d/T_u$ of the plasma as a whole is included.

Gaussian units),

$$\frac{d\rho}{dt} + \rho\nabla\cdot\boldsymbol{u} = 0 \tag{1}$$

$$\frac{d}{dt}\left(\frac{\boldsymbol{B}}{\rho}\right) = \frac{\boldsymbol{B}}{\rho}\cdot\nabla\boldsymbol{u} - \frac{1}{\rho}(\nabla\times\eta\boldsymbol{J}) \tag{2}$$

$$\frac{4\pi\boldsymbol{J}}{c} = \nabla\times\boldsymbol{B} \tag{3}$$

$$\rho\frac{d\boldsymbol{u}}{dt} = -\nabla\left(p + \frac{\boldsymbol{B}^2}{8\pi}\right) + \left(\nabla\cdot\frac{\boldsymbol{BB}}{4\pi}\right) + \nabla\lambda\rho\nabla\cdot\boldsymbol{u} - \nabla\cdot\mu\rho\boldsymbol{\Pi} \tag{4}$$

$$\rho\frac{de}{dt} = -p\nabla\cdot\boldsymbol{u} + \lambda\rho(\nabla\cdot\boldsymbol{u})^2 + \mu\rho(\boldsymbol{\Pi}\cdot\boldsymbol{\Pi}) + \eta(\boldsymbol{J}\cdot\boldsymbol{J}), \tag{5}$$

where ρ is the mass density, $\boldsymbol{B}$ is the magnetic field, $\boldsymbol{J}$ is the current density, c is the speed of light, $\boldsymbol{u}$ is the fluid velocity, e is the specific internal energy, and p is the fluid pressure. The symmetric rate-of-strain tensor, $\boldsymbol{\Pi}$, is defined as

$$\boldsymbol{\Pi} = \frac{1}{2}\left(\nabla\boldsymbol{u} + \nabla\boldsymbol{u}^{\mathrm{T}}\right). \tag{6}$$

The system is closed by the equation of state $p = e(\gamma - 1)\rho$ (where $\gamma = 5/3$ is the polytropic index) and the divergence-free condition, $\nabla\cdot\boldsymbol{B} = 0$, is imposed as an initial condition and maintained throughout the computation. The transport coefficients are the kinematic shear viscosity μ, the kinematic bulk viscosity λ and the resistive diffusivity η.

The FLIP-MHD method assigns the plasma properties to an arbitrary number of particles and computes the evolution of the system by solving a finite-difference discretization of the equations of motion

$$\frac{d\boldsymbol{x}_p}{dt} = \boldsymbol{u}_p \tag{7}$$

$$m_p\frac{d\boldsymbol{u}_p}{dt} = \boldsymbol{F}_p, \tag{8}$$

where $\boldsymbol{u}$, m, and $\boldsymbol{F}$ are the velocity, mass, and force acting on each particle p. The quantities $\boldsymbol{u}_p$ and $\boldsymbol{F}_p$ are computed, at each iteration, by solving the macroscopic system of equations with an implicit finite-difference discretization on a Lagrangian grid. The initial conditions for the grid quantities are computed by interpolating the particle properties on the Lagrangian grid through specific interpolation methods, either trilinear (for kinematic variables) or triquadratic (for thermodynamic variables) and a tensor product of b-splines. The interpolation procedure is extensively described in Brackbill & Ruppel (1986). One of FLIP-MHD's peculiarities is the choice to assign each particle a magnetic moment, from which a divergence-free magnetic field can be directly computed through the solution of a single Poisson's equation at each cycle (see Brackbill 1991 for a complete description). After advancing the grid properties in time, they are interpolated back to the particles to advance their position in the phase space, so that a new cycle can begin. More details on FLIP-MHD's features are listed in Brackbill & Lapenta (1998).

Using a Lagrangian grid in solving the macroscopic equations brings a series of advantages, such as "relaxed" CFL conditions (due to the necessity to control the zone edges overlapping) and the capability to handle great variations of the fluid density. Furthermore, the method is Galilean invariant: the motion of the fluid parcels introduces zero computational diffusion, as the mass flow is modeled through the particle motion through the grid. Instead, the interpolation steps do introduce numerical diffusion, but the overall diffusion is less important than high-order Eulerian methods.

The code is suitable to simulate realistic astrophysical phenomena, as it is robust enough to correctly compute the evolution of both stationary and unstable dynamical systems, as

well as shock and discontinuity formation and propagation. In this specific case, it is chosen to simulate a CME-like event and to compare it to observational data, restricting the domain to a 2D geometry. The simulated shock wave is let propagate in a realistic surrounding environment by imposing specific initial values of the unperturbed plasma parameters. Details on the CME initialization and simulation setup are presented in Section 4.1, while the results of the simulation are listed in Section 4.

3.2. "Modified" GrAALE: 1D, Lagrangian, Two-temperatures MHD

FLIP-MHD's one-fluid approach is sufficient to obtain simulation results concerning the properties of the plasma as a whole. However, to retrieve information on the behavior of the single particle species that are present in the plasma, a full two-fluid model should be adopted.

For this particular case of study, it is meaningful to apply a simpler model to assess the effects of the shock transit on the different particle species. In particular, when trying to model the energy gain and temperature decoupling of electrons and protons, a one-fluid, two-temperature ideal MHD model can be used to retrieve information for comparison with observations. This has been successfully done by other authors (see, e.g., van der Holst et al. 2010, Manchester et al. 2012, Sokolov et al. 2013) aiming at modeling the solar environment as accurately as possible, thus including many additional or observation-driven terms in the standard MHD equations. This introduces the necessary physics (such as particle collisions, Alfvén waves heating, etc.).

Here, we chose to develop two different approaches, using an upgraded version of the GrAALE code first presented in Finn et al. (2004) and Lapenta & King (2007). GrAALE is an arbitrary Eulerian–Lagrangian, grid adaptive method for MHD first developed by Giovanni Lapenta. For this application, only the Lagrangian part is used to solve the ideal MHD equations (in cgs units),

$$\frac{d\rho}{dt} = -\rho\nabla\cdot\boldsymbol{u} \tag{9}$$

$$\rho\frac{d\boldsymbol{u}}{dt} = -\nabla p + \frac{(\boldsymbol{B}\cdot\nabla)\boldsymbol{B}}{4\pi} - \nabla\left(\frac{\boldsymbol{B}^2}{8\pi}\right) \tag{10}$$

$$\rho\frac{de}{dt} = -p\nabla\cdot\boldsymbol{u} \tag{11}$$

$$\rho\frac{d}{dt}\left(\frac{\boldsymbol{B}}{\rho}\right) = (\boldsymbol{B}\cdot\nabla)\boldsymbol{u}, \tag{12}$$

where the notation is the same as used in Section 3.1. For the aim of this work, the code is set to solve the 1D ideal MHD equations, thus the divergence-free condition $\nabla\cdot\boldsymbol{B} = 0$ is satisfied by simply choosing a frame of reference where B_x is a constant. The equation of state $p = e(\gamma - 1)\rho$ again closes the system.

As stated in Manchester et al. (2012), the electrons and protons are expected to behave differently when subjected to a shock transit, because of their different thermal velocities. In particular, the electrons should not receive the heating due to kinetic energy dissipation at the shock front, since not even the fastest CME-driven shocks travel faster than the electron thermal speed. Thus, the electron temperature increase should only be related to the shock compressivity (following an adiabatic gas law) and secondary effects. The protons, instead, are expected to be heated by both the shock pressure jump and the kinetic energy dissipation and thus the proton temperature increase should be higher. The related properties of the plasma as a whole (total pressure and average temperature) still respect the standard hydromagnetic RH jump conditions.

When trying to model this behavior for the two species, it is possible to assume a very simple solar wind model, which comprises the ideal MHD equations and two separate energy equations replacing Equation (11), namely

$$\frac{dp_e}{dt} = -\gamma p_e\nabla\cdot\boldsymbol{u} \tag{13}$$

$$\rho\frac{de_p}{dt} = -p_p\nabla\cdot\boldsymbol{u} \tag{14}$$

where p_e and p_p are the electron and proton pressures, and e_p is the proton internal energy. The model adopted here is a reformulation of the one used in van der Holst et al. (2014), where all the additional terms have been neglected (since the simulation is run in a domain of negligible length compared to the typical length of evolution of secondary phenomena). The equation of state, $p_p = e_p(\gamma - 1)\rho$ is assumed to compute the proton pressure and the total pressure is given by $p = p_e + p_p$. The value of γ is set to 5/3 for both species, and it is assumed that electrons and protons move at the same velocity $\boldsymbol{u}$.

Since the ideal MHD energy equations do not contain dissipative terms, the standard approach to handle the shock energy release is to introduce account the so-called "artificial viscosity" q. Here, we choose to compute it according to the Kuropatenko formula (see, e.g., Caramana et al. 1998) and add it as an extra pressure term in both the momentum and energy equations. To model the behavior of the two different species we choose to add the artificial viscosity term to the proton energy equation and to leave unchanged the electron pressure equation. In this way, the electrons experience only adiabatic heating due to the shock compressivity. This can be easily shown by substituting Equation (9) into (13) and integrating in time: if no dissipative terms are added, the pressure jump between two generic states 1 and 2 is expressed by $p_2/p_1 = (\rho_2/\rho_1)^\gamma$. The associated temperature jump is, consequently, $T_2/T_1 = (\rho_2/\rho_1)^{\gamma-1}$, which is nothing else than the standard adiabatic compression law. The protons, instead, also receive the energy dissipated at the shock front, thanks to the action of the artificial viscosity. The plasma as a whole still experiences an energy jump according to the RH conditions.

Despite the fact that the model is designed to reproduce exactly the energy decoupling mechanisms named above, it has to be said that it neglects many physical phenomena that play a role in the shock propagation phenomenology. Moreover, it makes no distinction between the two particle species, as it does not contain any physical parameter introducing information about their different nature, but it only relies on the artificial viscosity effect, which is a purely computational entity.

To implement a model which is capable of introducing at least some features of the missing physics, while retaining the simplicity of the ideal MHD equations, we choose to adopt a slightly different approach to the energy evolution of the single

species. By substituting Equation (13) with

$$\rho \frac{de_e}{dt} = -p_e \nabla \cdot \boldsymbol{u} \tag{15}$$

the electrons are now treated in the same way as the protons, while avoiding the introduction of an artificial viscosity term. The different properties of the two species are now taken into account in the equations of state, $p_e = e_e(\gamma_e - 1)\rho$ and $p_p = e_p(\gamma_p - 1)\rho$, where the polytropic indices are now assumed to have different values. The total plasma pressure to be used in the other equations is still computed as the sum of the two partial pressures.

This simple variable γ model requires to properly choose the values of the polytropic indices for the two species. This can be done by relying on empirical data (see, e.g., Gosling 1999), trying to find realistic values that best conserve both the total plasma pressure and the average temperature jump (where $\bar{T}_d = (T_{e,d} + T_{p,d})/2$ is the average downstream plasma temperature). These values of γ are retrieved by measurements, and therefore they are determined by all the phenomena occurring during a shock transit. Thus, the introduction of such realistic parameters should bring the missing physics into the system, which cannot be modeled by the ideal MHD equations without additional terms.

One drawback of such a model is that it prevents us from computing the energy jump of the single species in advance. Evaluating the pressure equation for a single species s,

$$\frac{dp_s}{dt} = -\gamma_s p_s \nabla \cdot \boldsymbol{u}, \tag{16}$$

it has to be noted that there is no way to express it in a conservative form in order to obtain an equivalent of the RH jump conditions. Thus, the increase in the energy of the single species is not predictable and may give unphysical results if the value of γ_s is not chosen attentively. Nevertheless, it is possible to predict how the ratio between the energy of the species behaves when a shock propagates in the domain. Expanding the total derivative in Equation (16) yields

$$\frac{\partial}{\partial t}\left(\ln p_s\right) + \gamma_s \nabla \cdot \boldsymbol{u} + \boldsymbol{u} \cdot \nabla \ln p_s = 0. \tag{17}$$

Writing such an equation for electrons and protons separately and subtracting the second one from the first gives, in terms of total derivatives,

$$\frac{d}{dt}\left(\ln \frac{p_e}{p_p}\right) = -(\gamma_e - \gamma_p)\nabla \cdot \boldsymbol{u}, \tag{18}$$

which implies that the pressure ratio of the two species increases or decreases depending on the values of the polytropic indices and on the divergence of the velocity. At the shock front, where $\nabla \cdot \boldsymbol{u} < 0$, the ratio increases if $\gamma_e > \gamma_p$ and decreases if $\gamma_e < \gamma_p$, while it remains constant if the two indices have the same value. This allows us to verify the validity of the results, as it states that the species whose value of γ is higher experiences the highest relative energy increase. The results of the application of the two models is presented in Section 5.

4. FLIP-MHD RESULTS AND COMPARISON WITH WHITE LIGHT SPECTROSCOPICAL OBSERVATIONS

4.1. System Initialization

The cylindrical 2D computational domain represents a portion of the solar equatorial plane, 30° of latitude wide and 1 solar radius high (from 1.5 $R_\odot$ on the lower boundary to 2.5 $R_\odot$ on the upper boundary). A fixed number of particles is distributed over the domain according to the initial particle density profile (see below). The equations are solved in a Cartesian frame of reference (x, z), with 100 cells on both directions. The time step is set to 0.1, and the simulation is run up to $102\Delta t$. Figure 1 shows the geometry of the domain and the relations between the coordinates.

The Cartesian components of both velocity and magnetic field are computed by transforming the relative components on a 2D cylindrical frame of reference. The magnetic field is purely radial, initially, according to the expression found in Gombosi (2004), $B_r = 1.0R_0/(R_0 + z)$ (where $R_0 = 1.5R_\odot$) and $B_\phi = 0$. The transformation to Cartesian coordinates yields

$$B_x = B_r \sin\phi + B_\phi \cos\phi \tag{19}$$

$$B_z = B_r \cos\phi - B_\phi \sin\phi, \tag{20}$$

while keeping $B_y = 0$. The polar angle is given by $\phi = \sin^{-1}(x/\sqrt{(R_0 + z)^2 + x^2})$. As for the values of the velocity components, in cylindrical coordinates the initial values are uniformly set to $u_r = 0.1$ and $u_\phi = 0.1$. The change of frame of reference for u_x and u_z is made as already shown for the magnetic field.

The energy parameters are initialized according to semi-empirical laws expressing the particle density and temperature as a function of the radial distance from the solar surface. From Gibson et al. (1999) and Vásquez et al. (2003), the initial profiles are

$$n = 10^8\left(\frac{77.1}{h^{31.4}} + \frac{0.954}{h^{8.31}} + \frac{0.55}{h^{4.63}}\right)\left[\mathrm{cm}^{-3}\right] \tag{21}$$

$$T = 8 \times 10^5 \frac{a_{\mathrm{eq}}}{a_{\mathrm{eq}} + b_{\mathrm{eq}} h^{\alpha_{\mathrm{eq}}} + \left(1.0 - b_{\mathrm{eq}}\right)/h^{\beta_{\mathrm{eq}}}}[\mathrm{K}] \tag{22}$$

where $a_{\mathrm{eq}} = 0.1$, $b_{\mathrm{eq}} = 0.33$, $\alpha_{\mathrm{eq}} = 0.55$, $\beta_{\mathrm{eq}} = 6.6$. The initial plasma pressure is computed from the ideal gas law as $p = 2nk_{\mathrm{B}}T$ (where k_{B} is the Boltzmann constant), assuming $\gamma = 5/3$.

The CME is initialized at the lower boundary of the domain, following a standard approach in which a disequilibrium plasma blob with different pressure and velocity is injected (see, e.g., Chané et al. 2005 and Jacobs et al. 2005). At $t = 12\Delta t$, the new values of the parameters are set to

$$p_b' = p_b\left[1.0 + 0.5 \exp\left(-\left(\frac{x - x_c}{L_{x,b}/30.0}\right)^2\right)\right] \tag{23}$$

$$u_{x,b}' = u_{x,b} + 1.5c_{\mathrm{ms}} \exp\left(-\left(\frac{x - x_c}{L_{x,b}/30.0}\right)^2\right), \tag{24}$$

where p_b and $u_{x,b}$ are the initial values of pressure and x-velocity along the lower boundary, x_c is the x-coordinate of the domain center. L_x is the spatial length of the lower

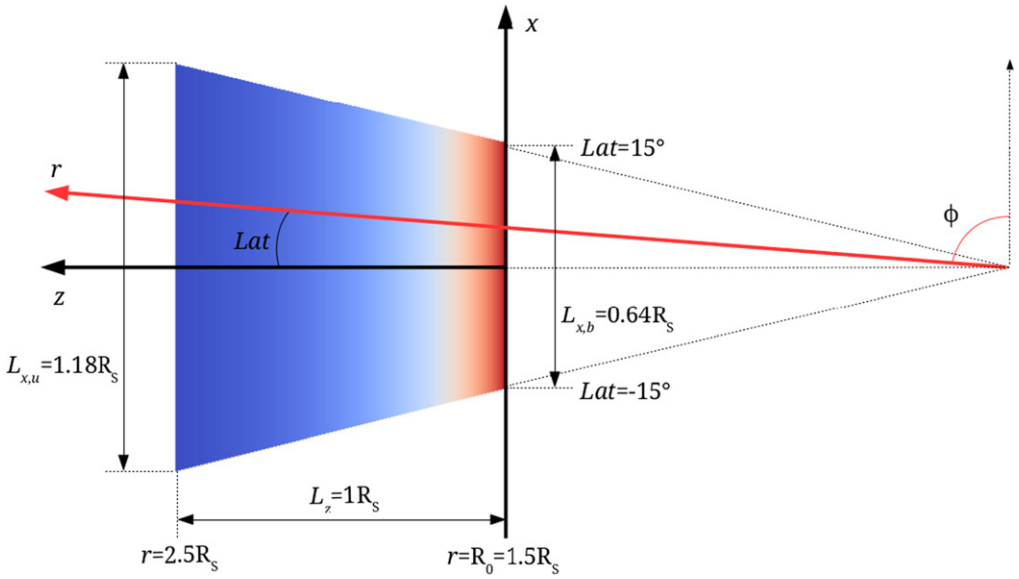

Figure 1. Geometrical relations between the cylindrical (r, ϕ) and Cartesian (x, z) coordinate systems. In the next figures, the coordinate system axes and scales are omitted.

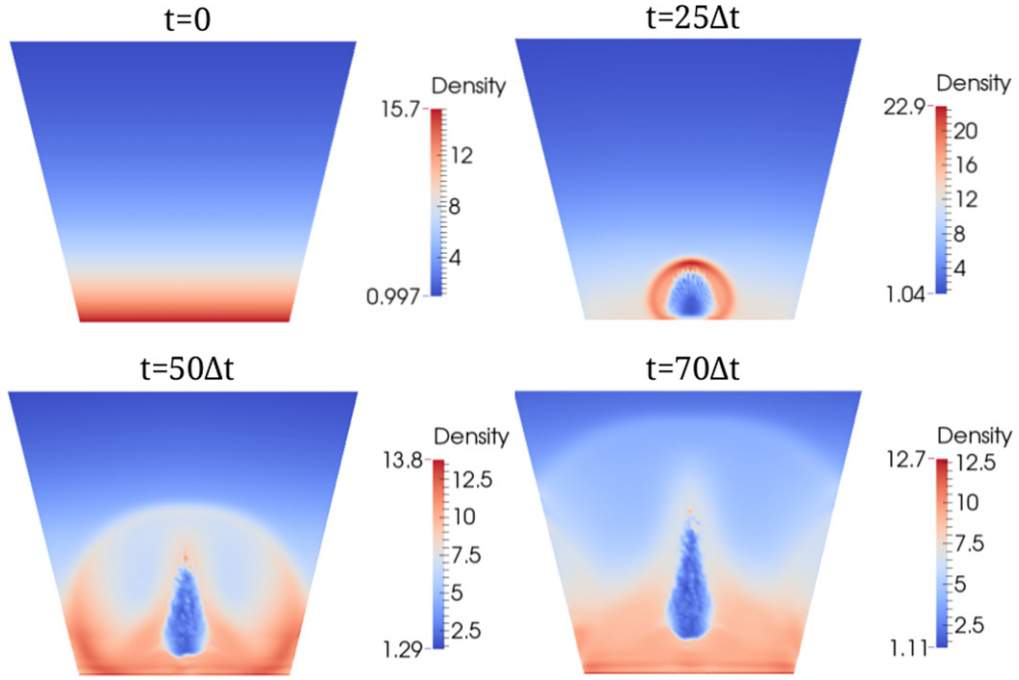

Figure 2. Snapshots of the simulated CME propagation with time. The coloring of the domain represents the value of the density, with redder zones pointing to higher values and bluer zones pointing to lower values. The CME front is clearly visible as it propagates through the unshocked medium.

boundary along the x-direction, and $c_{\rm ms}$ is the magnetosonic speed given by

$$c_{\rm ms} = \sqrt{\left(B_{x,b}^2 + B_{z,b}^2\right)\big/\rho_b + \gamma p_b\big/\rho_b} \tag{25}$$

with $B_{x,b}$, $B_{z,b}$, ρ_b the initial values of the magnetic field components and mass density along the lower boundary.

The transport coefficients are uniform in the domain and kept constant throughout the computation. They are computed from typical values of the dimensionless parameters for CME simulations (see, e.g., Lapenta & Knoll 2005, Lapenta & Lazarian 2012). The resistivity corresponds to a Lundquist number, $S = 4\pi L_z v_{{\rm A},b}\big/\eta = 10^3$, where $v_{{\rm A},b} = B_b\big/\sqrt{4\pi\rho_b}$ is the initial Alfvén velocity along the lower boundary. The kinematic shear viscosity corresponds to a viscous Reynolds number, $R = \rho_b L_z v_{{\rm A},b}\big/\mu = 10^3$, and the kinematic bulk viscosity is set as $\lambda = \mu$.

4.2. Simulation Results and Comparison with Observations

Figure 2 shows the evolution of the CME with time, from the growing phase to the damping due to its motion through the unshocked medium.

As a first analysis, simulation data relative to the time instant $t = 50\Delta t$ have been extracted from the code output and visualized with both Paraview and Matlab. Figure 3 shows the

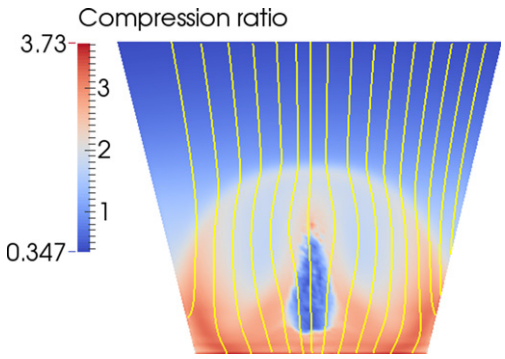

Figure 3. Simulation results at $t = 50\Delta t$. The compression ratio value is obtained, for this picture, by dividing the density at each point by the density of a specific point located at $x = L_{x,b}/2$, $z = L_z/3$.

spatial distribution of the compression ratio (obtained by dividing the downstream density values by the upstream values) at the selected time step, along with a few magnetic field lines displaying the deflection caused by the shock transit. The picture already evidences some agreements with observational results (see Paper I), specifically the highest density increase at the shock front nose (excluding the regions at the shock flanks where boundary effects are dominant) and the highest magnetic field deflection toward the shock flanks.

For more quantitative comparison, it is necessary to analyze the spatial distribution of the three major parameters of interest, namely the compression ratio, the magnetic field deflection, and the Alfvénic Mach number along the shock front. The analysis is carried out for the fully developed CME at three selected positions of the shock front nose during the propagation in the computational domain.

First of all, the shock front can be located on the 2D map by selecting a control parameter, such as pressure, and retrieving the position at which it assumes peculiar values caused by the shock front presence (specifically, the pressure should be highest). The coordinates of the shock front points give the exact location where to retrieve the values of the variables of interest. In this way, the density, magnetic field, and velocity components along the shock front are immediately available.

To compute the compression ratio, it is necessary to retrieve the value of the pre-shocked plasma density. This is far from easy, in this specific case, since it involves locating the position of the shock front "foot" points. There are several ways to accomplish this task. The standard approach consists of taking the values of the density relative to the same shock front points, but at $t = 0$; however, this method implies that we assume that the shock thickness is infinitesimal, which is not realistic. It is also possible to manually select the pre-shock points on the density distribution map, although this is, obviously, time-consuming and quite arbitrary, as it relies on ones capability to guess the shock front "foot" distance from the shock front itself.

Here, we refer to the results from Eselevich & Eselevich (2011, 2012), where it is shown that, below six solar radii from the Sun surface, the shock thickness is of the same order of the proton–proton mean free path λ_p, thus the shock is collisional. The value of λ_p can be estimated with the semi-empirical expression proposed in Zel'dovich & Raizer (1966),

$$\lambda_p = 10^{-7}\frac{T^2}{n}[R_\odot], \tag{26}$$

where T and n are the plasma temperature (in K) and particle density (in cm^{-3}). Then, we define the shock thickness as $\delta_{\mathrm{sh}} = k\lambda_p$, where k is an empirical coefficient whose value can be adjusted to take into account that the more the shock propagates from the source surface, the less collisional it becomes (thus diminishing its thickness). As underlined by Eselevich (2010), a good estimate for the shock thickness at the nose, when this reaches the height $h = 2R_\odot$, is $\delta_{\mathrm{sh}} \simeq 0.2R_\odot$. In the same paper, it is stated that the shock front thickness increases with the distance from the Sun surface, until the shock reaches a height of $\sim 6R_\odot$, where it abruptly becomes much smaller than λ_p. However, the limited box size, and thus the small differences in distance between the positions at which we analyze the results, allow us to neglect the increase in the shock thickness. Therefore, at each position we adjust the parameter k so that $\delta_{\mathrm{sh}} \simeq 0.2R_\odot$ at the shock nose. The pre-shock points are located, on the 2D map, starting from each shock front point and following the direction of the shock front normal for a distance of δ_{sh}, thus retrieving the pre-shock density values.

The inclination of the shock front normal at each point can be retrieved knowing the position of the shock front points on the 2D map. An interpolation curve can be drawn as a best fit nth order polynomial, to represent the shock front with a mathematical function with a known derivative, whose values are equal to the slope of the tangent at each point of the shock front.

To compute the magnetic field deflection, there is no need to know the actual pre-shock magnetic field components. With the provided assumption of initial radial magnetic field, the pre-shock angle ϕ can be retrieved from geometrical considerations, as shown in Figure 1. The total magnetic field deflection is simply given by

$$d = \phi - \tan^{-1}\frac{B_{z,s}}{B_{x,s}} \tag{27}$$

where $B_{z,s}$ and $B_{x,s}$ are the magnetic field components along the shock front.

Finally, the Alfvénic Mach number along the shock front is easily computed from the standard expression

$$M_{\mathrm{A}} = \frac{u_s}{u_{\mathrm{A},s}} \tag{28}$$

where u_s and $v_{\mathrm{A},s} = B_s/\sqrt{\mu_0 \rho_s}$ are the plasma velocity and Alfvén speed along the shock front (in a frame of reference at rest with the Sun), with B_s and ρ_s being the relative magnetic field and plasma density.

Figure 4 shows the spatial distribution of the three parameters along the shock front, at different times during the shock propagation. As expected from observations (see Paper I), the compression ratio and Alfvénic Mach number are higher at the shock nose, while the magnetic field deflection is zero at the shock nose and increases gradually, reaching a maximum value at specular points toward the shock flanks. For comparison, see Figure 5 for the observed Alfvénic Mach number (left panel) and magnetic field deflection (right panel). Finally, it has to be noted that the shocks loses strength (in terms of compression ratio) as it propagates through the unshocked medium, which is again in agreement with observations.

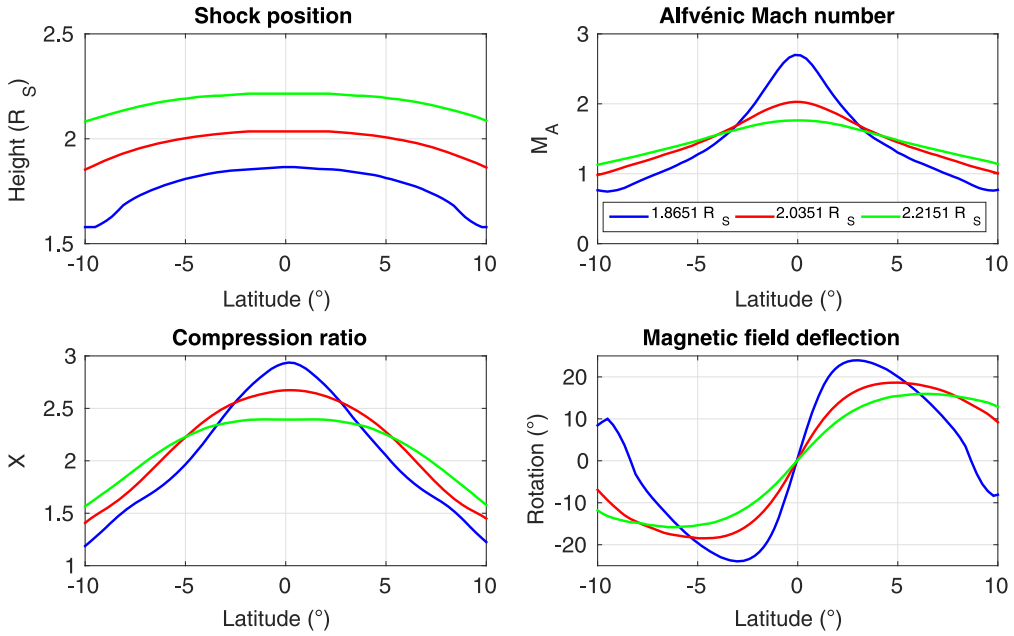

Figure 4. Magnitude of the physical variables of interest, along the shock front, at different times during the CME propagation. The shock nose position (latitude = 0°) is taken as a reference for the whole shock distance from the Sun surface. The domain latitude boundaries have been cut to avoid taking into account boundary effects.

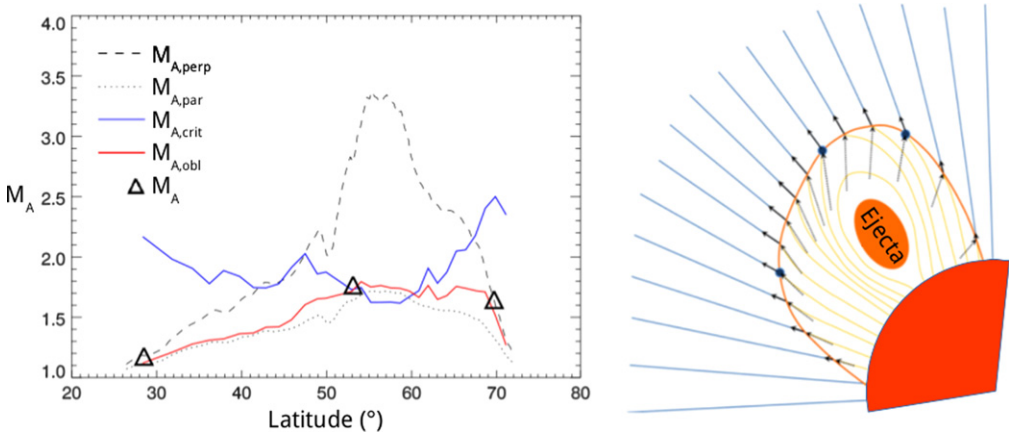

Figure 5. Left panel: observed values for the Alfvénic Mach number in the case of perpendicular (dashed black line) and parallel (dotted black line) shocks, together with values for the critical Mach number (solid blue line) and for oblique shocks (solid red line). Right panel: a diagram showing a possible 2D distribution of magnetic field lines. Pre-shock magnetic and velocity vectors are drawn along radials (blue lines), while inclinations of post-shock magnetic field (yellow lines) and velocity vectors (black arrows) with respect to the shock surface corresponds to what was measured for the three points analyzed here (see Section 5). Inclinations of vectors at other locations along the front have been drawn by imposing continuity. Both figures are based on data taken from Paper I.

It is also interesting to apply a more in-depth analysis to the retrieved values of the Alfvénic Mach number. The relation between $M_{\rm A}$ and X, for $\gamma = 5/3$, is given by the shock adiabatic equation (see, e.g., Mann et al. 1995)

$$\left(M_{\rm A}^2 - X\right)^2\left[5\beta_u X + 2M_{\rm A}^2\cos^2\theta_{Bn}\left(X-4\right)\right] + M_{\rm A}^2 X\sin^2\theta_{Bn}\left[\left(5+X\right)M_{\rm A}^2 + 2X\left(X-4\right)\right] = 0, \quad (29)$$

where $\beta_u = 2\mu_0 p_u/B_u^2$ is the plasma-to-magnetic pressure ratio, with p_u and B_u being the upstream plasma pressure and magnetic field. θ_{Bn} is the angle between the upstream magnetic field and the shock front normal.

In the particular case $\theta_{Bn} = 0$ (parallel shock), solving the above for $M_{\rm A}$ gives two distinct solutions, namely

$$M_{\rm A,\parallel} = \sqrt{X}, \qquad M_{\rm A,\parallel} = \sqrt{\frac{5\beta_u X}{2(4-X)}}, \quad (30)$$

with the second one holding only in the case $\beta_u \neq 0$. When considering the case $\theta_{Bn} = \pi/2$ (perpendicular shock), the shock adiabatic reduces to

$$M_{\rm A,\perp}^4\left(X + 5\beta_u + 5\right) + M_{\rm A,\perp}^2 2X \times \left(X - 5\beta_u - 4\right) + 5\beta_u X^2 = 0, \quad (31)$$

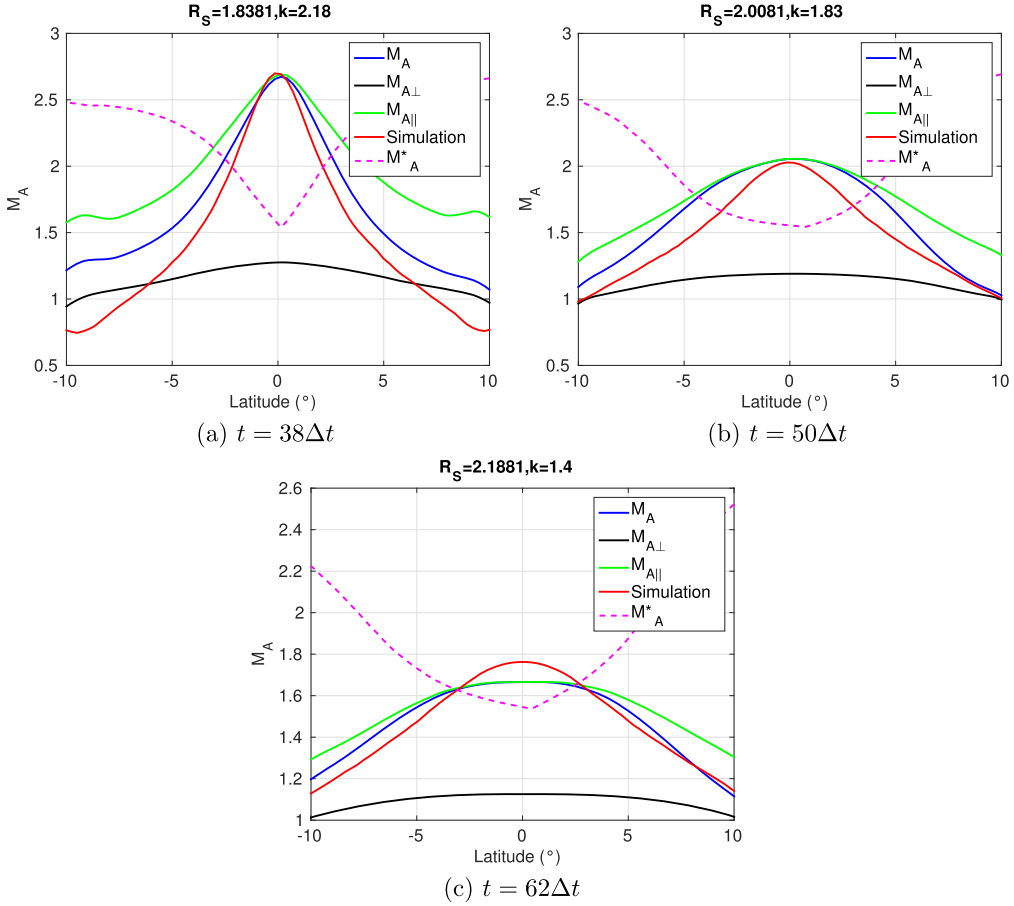

(a) $t = 38\Delta t$ (b) $t = 50\Delta t$

(c) $t = 62\Delta t$

Figure 6. Alfvénic Mach number along the shock front at different times during the shock propagation. The red lines show the actual values as retrieved from the simulation, compared to the values from the semi-empirical relation (blue lines) and the solutions of the shock adiabatic equation for a parallel (green lines) and perpendicular (black lines) shock. For the latter, out of the four possible solutions, two are negative (not physically relevant) and the other two present negligibly different values, thus either can be chosen. The dotted line shows the variation of the critical Alfvénic Mach number.

which in general gives four distinct solutions (depending on the values of X and β_u). In the case $\beta_u \simeq 0$, the solution is simply

$$M_{\mathrm{A},\perp} = \sqrt{\frac{2X\,(4 - X)}{X + 5}}\,. \tag{32}$$

As underlined in Bemporad & Mancuso (2011), the actual values of M_A along the shock front, for a generically oblique shock, can be well approximated by the semi-empirical expression

$$M_{\mathrm{A},\angle} = \sqrt{\left(M_{\mathrm{A},\perp}\sin\theta_{Bn}\right)^2 + \left(M_{\mathrm{A},\parallel}\cos\theta_{Bn}\right)^2}\,, \tag{33}$$

which only relies on the value of the compression ratio, X, and θ_{Bn}, whose values are given by the difference between the angles of inclination of the shock front normal (used to locate the pre-shock density) and the upstream magnetic field (known from previous geometrical analyses). It is interesting to compare the values of M_A obtained with the semi-empirical expression with the actual values along the shock front as produced by the simulation. In this specific case, it is not possible to assume the condition $\beta_u \simeq 0$, thus the values of $M_{\mathrm{A},\parallel}$ and $M_{\mathrm{A},\perp}$ are computed according to the expressions which include the effect of the plasma-to-magnetic pressure ratio. The comparison is shown in Figure 6.

Another comparison to be carried out concerns the supercriticality of the shock propagation. This is determined by the condition $M_\mathrm{A} > M_\mathrm{A}^*$, where M_A^* is the critical Alfvénic Mach number, the threshold value below which the downstream plasma velocity is subsonic. The implications of the shock supercriticality, as denoted in Bemporad & Mancuso (2011), include the possibility to produce SEPs through ion reflection across the shock front and electron acceleration up to the energy range relevant for the production of type II bursts in the solar corona. Critical values of M_A are provided by Edmiston & Kennel (1984) as a function of θ_{Bn}, for collisionless non-relativistic shocks. The spatial distribution of the critical Alfvénic Mach number is reported again in Figure 6.

The results can be compared with Figure 5. First of all, it is evident that the values relative to a parallel shock (green line) best approximate the actual M_A values at the shock nose, where the shock almost behaves as purely parallel. At the flanks, the shock loses this peculiarity and the values relative to a perpendicular shock (black line) are better in approximating the actual M_A values. The combination of the two through the semi-empirical relation (blue line) is therefore quite accurate in reproducing the simulation results. Moreover, it has to be noted that as the shock propagates through the domain, it becomes more and more similar to a parallel shock also outside of the nose zone, thus the perpendicular values get less and less important in approximating the distribution of the actual M_A.

At the same time, the value of the coefficient k used to adjust the shock thickness δ_{sh} decreases, meaning that the shock is getting less collisional, which is expected from observations. Finally, it is evident that the shock is supercritical in a certain area around the nose, which becomes smaller during the propagation in the unshocked medium. This is again in agreement with what reported in Bemporad & Mancuso (2011).

5. MULTI-TEMPERATURE MODELS RESULTS

5.1. System Setup

The analysis is carried out in a 1D geometry, through a conversion to a frame of reference such that the x-direction is parallel to the shock front normal. The values of the plasma parameters at specific points along the shock front of the CME event taken as a reference are used for comparison with observations. The initial conditions of the problem have been set in the same way as for a standard shock tube test, taking the upstream and downstream values relative to points 1, 2, and 3 from Table 1.

In a standard 1D, single-temperature approach, imposing these values as initial conditions on the domain would produce no more than a pure shock propagation, as they respect the RH jump conditions. The shock wave would travel with a speed equal to the sum of the magnitude of the projections of the velocity vectors $\boldsymbol{u}$ and $\boldsymbol{u}_{out}$ over the shock normal direction. No expansion waves or secondary discontinuities would appear. However, when using the simple solar wind model the sudden jump in the values due to the shock transit is not predictable (as underlined in Section 3.2). Thus, for consistency, it is chosen to impose the same upstream and downstream values for all the quantities, with the expectation to find secondary discontinuities in the results. The total pressure is subdivided between electrons and protons as $p_e = p_i = p/2$, which is true for the upstream region (as the two species are assumed to have the same temperature) but certainly not true for the downstream region, due to the different values of γ. Thus, the initial ratio p_e/p_i is set to 1. The temperature of each species is computed from the ideal gas law as $p = nk_B T$.

As a first test, the initial conditions relative to point 3 are imposed for the variable γ-model. The system is let to evolve, with three different settings: $\gamma_e = \gamma_i = 5/3$, $\gamma_e = \gamma_i + 0.1$, and $\gamma_e = \gamma_i - 0.1$. The simulation is performed in a domain of length $L = 1$ m, with a resolution of 400 cells and a time step computed automatically at each iteration to avoid numerical instabilities, up to the final time 1.5×10^{-7} s.

As reported in Gosling (1999), realistic values of the polytropic index for electrons are in general lower than the values for protons. Specifically, the realistic range for γ_e varies from 1.13 to 1.33, while γ_p ranges from 1.35 to 1.57. To evaluate the effect of the different values of γ on the system evolution, the simulation is run up to the final time 3.0×10^{-7} s for each point and the results are compared to the ones obtained with the simple solar wind model introduced in Section 3.2.

5.2. Simulation Results

The results of the preliminary test are shown in Figure 7: as expected, the ratio p_e/p_i undergoes a sudden change due to the shock transit (if $\gamma_e \neq \gamma_i$), without the possibility to predict it.

Figure 8 shows the results of the application of the two models for Point 3 of the shock front, while Table 2 lists the values of the ratio T_d/T_u for both species and for the plasma as a whole, comparing the outcomes obtained with the different approaches.

The results show that both models can accurately conserve the average temperature jump $\bar{T}_d/T_u$ which is valid for the single-temperature model, as obtained with the RH jump conditions. As for the simple solar wind model, it is capable of distributing the energy of the shock transit between electrons and protons as expected from theory. Only the protons are heated by the kinetic energy dissipated at the shock front, while electrons undergo a pure adiabatic compression (which causes a much lower temperature increase, see, e.g., Manchester et al. 2012). This model, however, does not take into account any additional phenomena occurring during the shock transit. Instead, the variable γ-model only relies on the value of the polytropic index to distribute the energy among the various species. By imposing realistic values for both electrons and protons, the model again produces a decoupling of the temperatures, showing a higher temperature jump for the electrons and a lower one for the protons, with respect to the solar wind model. This is what is expected to occur in a CME event, where electrons should receive energy through secondary phenomena (such as thermal exchange with protons), while undergoing the main heating due to the shock compression. It is evident that inserting a proper value of γ allows us to introduce the missing physics in the problem, thus showing results which should more accurately model the behavior of the different species. Nevertheless, a full two-fluid model is still needed to obtain more precise results, although such a simple two-temperature model already shows encouraging outcomes which should push future efforts toward the same direction.

6. CONCLUSIONS

In this work we compare observational results first presented in Bemporad & Mancuso (2011) and further extended in Paper I relative to the 1999 June 11 CME event with simulation data. For this purpose two different approaches have been followed, in order to obtain information on the post-shock plasma parameter values. The first approach involves a one-fluid, 2D visco-resistive MHD PIC simulation of a CME expanding in the surrounding environment, run with FLIPMHD3D. Here, the unshocked medium properties have been set according to realistic profiles found in Vásquez et al. (2003). The second approach involves the analysis of specific points along the CME-driven shock front with a two-temperature, 1D, Lagrangian ideal MHD model. This is based on the GrAALE code written by Giovanni Lapenta. The main results of the two approaches can be summarized as follows.

1. The simulation run with FLIPMHD3D shows, at $t = 50\Delta t$, good agreement with observational results from Paper I: specifically, the highest compression ratio is found at the shock nose, while the strongest magnetic field deflection (assumed to be radial in the unshocked medium) occurs toward the shock flanks.
2. For more quantitative comparison, the values of X (compression ratio), d (magnetic field deflection), and M_A (Alfvénic Mach number) along the shock front are retrieved at the shock nose positions $1.84R_\odot$, $2.00R_\odot$, $2.19R_\odot$. To compute the upstream parameters, it is

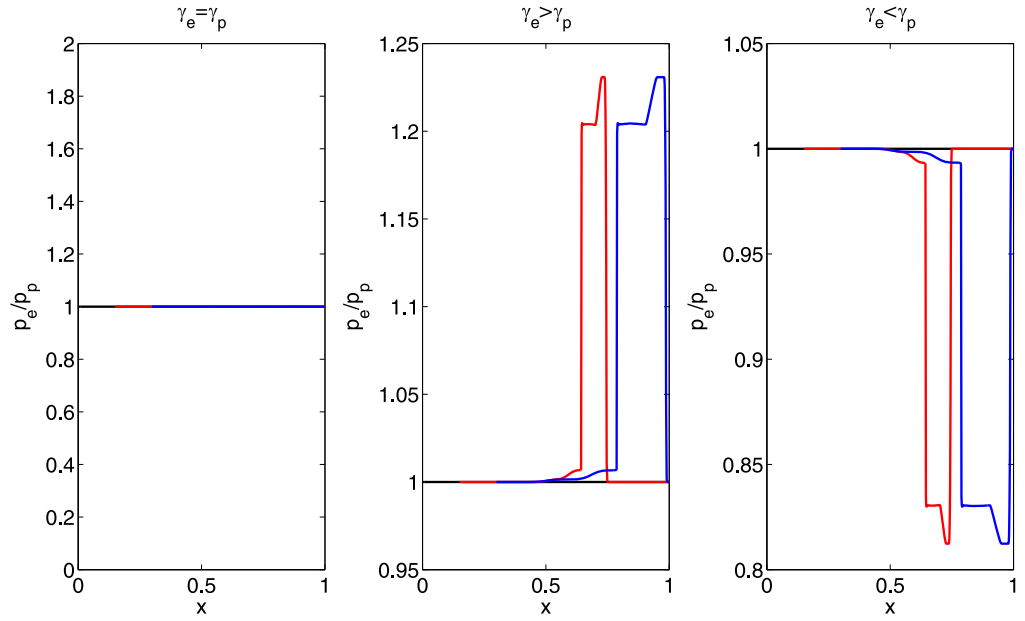

Figure 7. Plot of the spatial distribution of the ratio p_e/p_i, computed with the variable γ model, at different times. The initial condition (black line) is either constant, if $\gamma_e = \gamma_i$, or it undergoes a sudden increase or decrease (red lines for $t = 1.5 \times 10^{-7}$ s and blue lines for $t = 3.0 \times 10^{-7}$ s) in the zones of the domain where $\nabla \cdot \boldsymbol{u} < 0$, corresponding to the shock front.

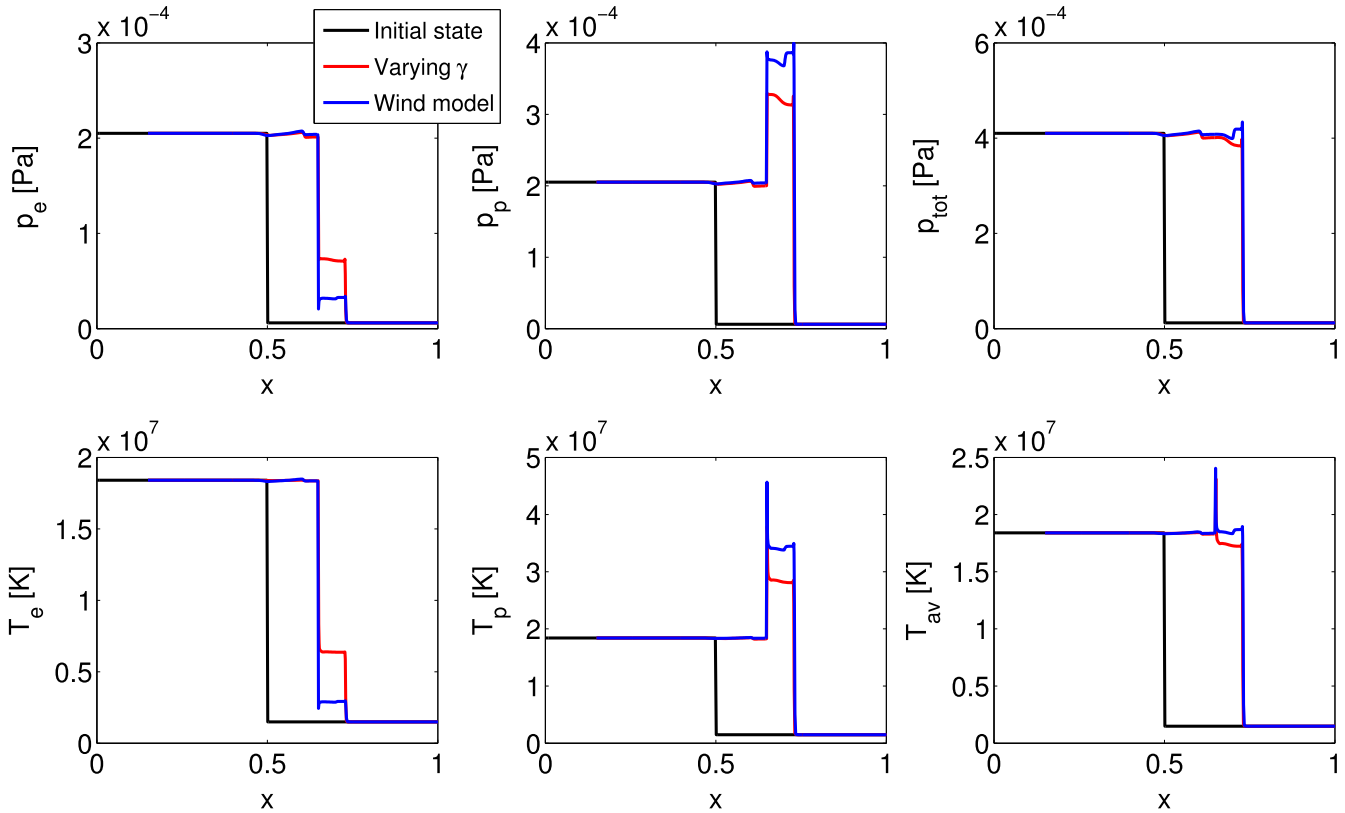

Figure 8. Comparison between the two models for Point 3 along the shock front. In both cases the pressure and temperature of the plasma as a whole, downstream of the shock, are conserved, while the two species undergo a decoupling in both parameters due to the different values of γ (for the variable γ model) and the different governing equations (for the solar wind model).

assumed that the shock front spans over a distance of the order of the proton–proton mean free path (computed according to the expression from Zel'dovich & Raizer 1966), adjusting it with a real coefficient k to take into account the shock loss of collisionality as it propagates in the surrounding environment. As expected from observations, the values of X and M_A remain higher at the shock nose during the CME propagation, while the magnetic field undergoes a deflection toward opposite directions at the two shock flanks.

3. Considering the spatial distribution of M_A along the shock front, this can be well approximated by the semi-empirical expression reported in Bemporad & Mancuso (2011). Specifically, the values of the Alfvénic Mach number relative to a parallel shock best fit the simulation result in an area around the shock nose, which spreads toward the flank at later times. This is due to how the shock is configured in the specific case, as it becomes more and more similar to a parallel shock at almost all the shock front points toward the end of the simulation. Moreover, comparing the values of M_A obtained from the simulation with the critical values M_A^* (retrieved from Edmiston & Kennel 1984), it shows that the shock is supercritical at the nose and subcritical at the flanks, confirming again the observations.
4. The two-temperature simulation run with the upgraded GrAALE is set up imposing the initial conditions of a standard shock tube test, taking the upstream values from Paper I relative to three points at different locations along the shock front. The downstream values are computed from the standard hydromagnetic RH jump conditions. Two different models are used to assess the electron–proton energy decoupling due to the shock transit.
5. As stated in Manchester et al. (2012), the electrons are expected not to receive energy dissipated at the shock front, because of their high thermal speed. Thus, a possible approach is to impose a pressure evolution equation for the electrons which does not introduce any dissipation mechanisms, leading to an electron heating only due to the shock compressivity. The protons, instead, are heated also by the shock dissipation of kinetic energy, thus undergoing a higher temperature jump. The model reproduces accurately what expected, but does not consider any other secondary mechanisms through which the electrons could receive energy (collisions, Alfvén waves, etc.).
6. Another possibility is to let both species' energy to evolve according to an equation which allows heating through the shock energy dissipation, but also includes the dependence on realistic values of the polytropic index γ. This is now set differently for electrons and protons, according to what reported in Gosling (1999); with this technique, the physics influencing the values of γ_e and γ_p is introduced in the system. The results obtained with such a model show that the electrons undergo a higher temperature jump with respect to the pure shock compressivity action, which is a more realistic behavior. In both models, the properties of the plasma as a whole (pressure and temperature) still respect the RH jump conditions.

The obtained results confirm what observed and validate the use of the semi-empirical expressions for the spatial distribution of M_A along CME-driven shocks. Moreover, it is shown that a simple 1D, two-temperature MHD model can already give interesting results about the different behavior of the electrons and protons subjected to the shock transit. More sophisticated models are still required for obtaining results with higher orders of accuracy, such as a full two-fluid model for simulating the electrons and protons behavior, or a multi-fluid model to include the effect on heavier ions present in the solar corona. This lays the basis for future works following the same direction. Nevertheless, it is evident that the introduction of realistic values in the governing equation parameters can better model the actual interactions occurring during the considered type of events. This opens another path to be followed in the future for gaining a deeper knowledge on the subject and develop a more and more accurate description of the nature of such phenomena.

Part of the research leading to these results has been carried out in the frame of the DEEP (Dynamically Exascale Entry Platform) project, which received funding from the European Community under Grant Agreement No. 287530. The simulations were conducted using computational resources provided by the PRACE Tier-0 Program. F.B. thanks B. Ripperda, D. Millas, and N. Magyar for useful discussions in the last phases of this work.

REFERENCES

Balan, N., Skoug, R., Tulasi Ram, S., et al. 2014, JGR, 119, 12
Bemporad, A., & Mancuso, S. 2010, ApJ, 720, 130
Bemporad, A., & Mancuso, S. 2011, ApJL, 739, L64
Bemporad, A., & Mancuso, S. 2013, JARe, 4, 287
Bemporad, A., Susino, R., & Lapenta, G. 2014, ApJ, 784, 102
Brackbill, J. U. 1988, JCP, 75, 469
Brackbill, J. U. 1991, JCP, 96, 163
Brackbill, J. U., & Ruppel, H. M. 1986, JCP, 65, 314
Caramana, E. J., Shashkov, M. J., & Whalen, P. P. J. 1998, JCP, 114, 70
Chané, E., Jacobs, C., van der Holst, B., et al. 2005, A&A, 432, 331
Cliver, E. W., Kahler, S., & Reames, D. 2004, ApJ, 605, 902
Edmiston, J. P., & Kennel, C. F. 1984, JPlPh, 32, 429
Eselevich, M. V. 2010, ARep, 54, 173
Eselevich, M. V., & Eselevich, V. G. 2011, ARep, 55, 1038
Eselevich, V. G., & Eselevich, M. V. 2012, ApJ, 761, 68
Finn, J. M., Lapenta, G., & Li, H. 2004, PhPl, 11, 2082
Forbes, T., Linker, J., Chen, J., et al. 2006, SSR, 123, 251
Gargaté, L., Fonseca, R. A., Silva, L. O., Bamford, R. A., & Bingham, R. 2014, ApJ, 792, 9
Giacalone, J. 2005, ApJL, 628, L37
Gibson, S. E., Biesecker, D., Guhathakurta, M., et al. 1999, ApJ, 520, 871
Gombosi, T. I. 2004, Physics of the Space Environment (1st edn.; Cambridge: CUP)
Gopalswamy, N. 2003, AdSpR, 31, 869
Gopalswamy, N., & Yashiro, S. 2011, ApJL, 736, L17
Gopalswamy, N., Thompson, W. T., Davila, J. M., et al. 2009, SoPh, 259, 227
Gosling, J. T. 1999, JGR, 104, 19851
Jacobs, C., Poedts, S., van der Holst, B., et al. 2005, A&A, 430, 1099
Jin, M., Manchester, W. B., IV, van der Holst, B., et al. 2012, ApJ, 745, 6
Jin, M., Manchester, W. B., van der Holst, B., et al. 2013, ApJ, 773, 50
Kahler, S. W. 2001, JGR, 106, 20947
Kim, R.-S., Gopalswamy, N., Moon, Y.-J., Cho, K.-S., & Yahiro, S. 2012, ApJ, 746, 118
Lapenta, G., & King, J. 2007, JGR, 112, A12204
Lapenta, G., & Knoll, D. A. 2005, ApJ, 624, 1049
Lapenta, G., & Lazarian, A. 2012, NPG, 19, 251
Lee, J.-O., Moon, Y.-J., Lee, J.-Y., et al. 2014, ApJL, 796, L16
Liu, Y. C.-M., Opher, M., Wang, Y., & Gombosi, T. I. 2011, A&A, 527, A46
Magdalenić, J., Marqué, C., Krupar, V., et al. 2014, ApJ, 791, 115
Manchester, W. B., van der Holst, B., Tóth, G., & Gombosi, T. I. 2012, ApJ, 756, 81
Mancuso, S., & Avetta, D. 2008, ApJ, 677, 683
Mancuso, S., Raymond, J. C., Kohl, J., et al. 2002, A&A, 383, 267
Mann, G., Claßen, T., & Auraß, H. 1995, A&A, 295, 775
Ontiveros, V., & Vourlidas, A. 2009, ApJ, 693, 267
Park, J., Moon, Y.-J., & Gopalswamy, N. 2012, JGR, 117, A08108
Powell, K. G., Roe, P. L., Linde, T. J., et al. 1999, JCP, 154, 284
Reiner, M. J., Vourlidas, A., Cyr, O. C., St., et al. 2003, ApJ, 590, 533
Schwartz, S. J., Henley, E., Mitchell, J., & Krasnoselskikh, V. 2011, PhRvL, 107, 215002
Sheeley, N. R., Hakala, W. N., & Wang, Y.-M. 2000, JGR, 105, 5081
Shen, C., Liao, C., Wang, Y., Ye, P., & Wang, S. 2013, SoPh, 282, 543
Sokolov, I. V., van der Holst, B., Oran, R., et al. 2013, ApJ, 764, 23
Tóth, G., Sokolov, I. V., Gombosi, T. I., et al. 2005, JGR (SpPh), 110, 12226
Treumann, R. A. 2009, A&ARv, 17, 409

van der Holst, B., Manchester, W. B., & Frazin, R. A. 2010, ApJ, 725, 1373
van der Holst, B., Sokolov, I. V., Meng, X., et al. 2014, ApJ, 782, 81
Vásquez, A. M., van Ballegooijen, A. A., & Raymond, J. C. 2003, ApJ, 598, 1361
Vourlidas, A., Wu, S. T., Wang, A. H., Subramanian, P., & Howard, R. A. 2003, ApJ, 534, 456
Vourlidas, A., Lynch, B. J., Howard, R. A., & Li, Y. 2013, SoPh, 284, 179
Zel'dovich, Y. B., & Raizer, Y. P. 1966, Physics of Shock Waves and High-Temperature Hydrodynamic Phenomena (1st ed.; New York: AP)